Nanoscale

Thermodynamically guided synthesis of 3R-TaSe$_2$ nanocrystals and their superconducting behavior

Mahmoud M. Hammo, [*a,b] M. A. A. Mohamed, [*a,c] Esam K. Moustafa, [a] Daniel Wolf, [a] Samuel Froeschke, [a] Ammar Soliman, [a] Joseph Dufouleur, [a] Romain Giraud, [a,d] Bernd Büchner, [a,e] Michael Mertig [b,f] and Silke Hampel [a]

Two-dimensional (2D) TaSe$_2$ has recently garnered significant attention due to its intrinsic physical properties, *e.g.*, charge density wave (CDW) states, Mott insulator transitions, and superconductivity. In this study, we optimized the synthesis conditions for preparing highly crystalline 3R-TaSe$_2$ using a chemical vapor transport (CVT) approach. We systematically investigated the influence of substrate type on the morphology of the resulting nanocrystals (NCs) and elucidated the underlying growth mechanisms. The NCs were grown on various substrates, including SiO$_2$/Si, *c*-sapphire (0001), and mica, under optimal conditions. The deposited crystals were characterized using various techniques, including optical microscopy (OM), atomic force microscopy (AFM), scanning electron microscopy (SEM), energy dispersive X-ray spectroscopy (EDX) and high-resolution transmission electron microscopy (HRTEM). In addition, magneto-transport measurements were carried out. Of particular interest, the prepared 3R-TaSe$_2$ NCs showed a signature of CDWs at around 100 K and an onset of superconductivity below 2.2 K. Such highly crystalline NCs are interesting for fundamental research of properties such as CDW phenomena and superconductivity at the nanoscale. This work provides insights into substrate-mediated growth and paves the way for advancing the knowledge of 2D TaSe$_2$ materials for potential applications in next-generation nanodevices.

Introduction

Two-dimensional (2D) metallic transition metal dichalcogenides (TMDs), such as TaS$_2$,[1–4] TaSe$_2$,[5–7] TiSe$_2$,[8–12] and NbSe$_2$,[13–16] have attracted significant research attention due to their diverse physical properties like superconductivity, charge density waves (CDWs), and metal–insulator transitions, making them particularly intriguing for fundamental studies and applications.[17] Multilayer TMDs have repetitive layers of X–TM–X, where TM and X represent transition metal and chalcogen, respectively. These materials commonly exhibit three basic possible stacking structures, including octahedral (1T), trigonal prismatic hexagonal (2H) and trigonal prismatic

rhombohedral (3R). More complex mixed-phase arrangements, such as 4H$_b$ and 6R, were also reported.[18–21] These stacking variations play a crucial role in governing phenomena such as CDWs, superconductivity, and quantum spin liquid behavior, making these materials an exciting platform for exploring novel electronic and quantum materials.[17] In particular, 3R stacked TMDs (Fig. 1a and b) show interesting properties due to their unique crystal structures and broken inversion symmetry, making them highly attractive for potential applications of nonlinear optical and ultrafast devices.[22–26]

Given the strong correlation between crystal quality and physical properties, it is crucial to synthesize highly crystalline pure 3R-TMD nanocrystals (NCs) using suitable growth methods. To date, 3R-TaSe$_2$ NCs or thin films have been prepared by various methods, including chemical vapor deposition (CVD),[27] molecular beam epitaxy (MBE),[28] and mechanical exfoliation from bulk crystals,[29,30] using a variety of substrates such as SiO$_2$/Si,[27] sapphire (Al$_2$O$_3$) or SiC.[28]

In general, the choice of substrates significantly influences not only the growth process but also the intrinsic properties of 2D materials such as the degree of charge transfer and mechanical stability, resulting in alterations in the carrier mobility and device operation.[31] Besides, the different nature of strain, caused by various substrates, can result in the

*a*Leibniz Institute for Solid State and Materials Research Dresden, Helmholtzstraße 20, 01069 Dresden, Germany. E-mail: m.hammo@ifw-dresden.de,
m.a.a.mohamed@ifw-dresden.de
*b*Institute of Physical Chemistry, Technische Universität Dresden, 01062 Dresden, Germany
*c*Department of Physics, Faculty of Science, Sohag University, 82524 Sohag, Egypt
*d*Université Grenoble Alpes, CNRS, CEA, Spintec, F-38000 Grenoble, France
*e*Institute of Solid State and Materials Physics, Technische Universität Dresden, 01062 Dresden, Germany
*f*Kurt-Schwabe-Institut für Mess- und Sensortechnik Meinsberg e.V., Kurt-Schwabe-Straße 4, 04736 Waldheim, Germany
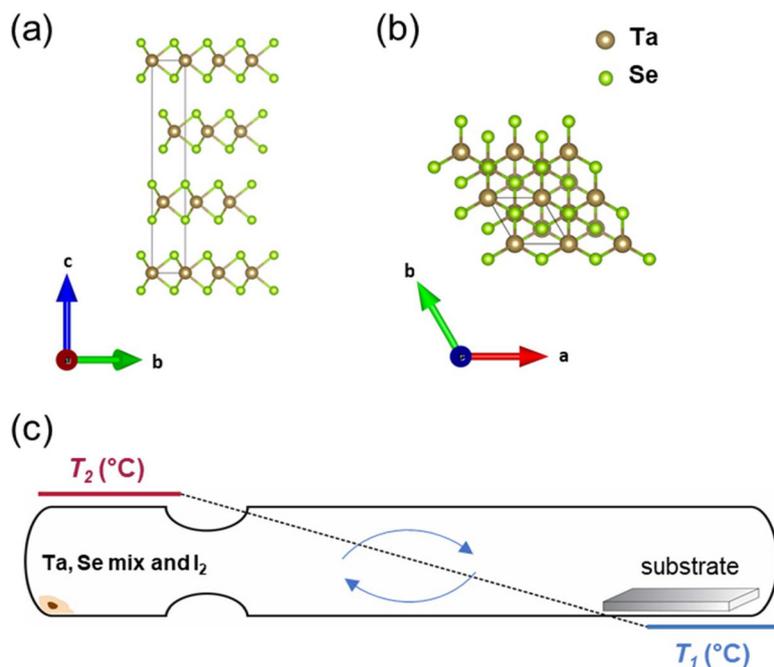
Fig. 1 (a) Schematic of the structural polytypes of 3R-TaSe$_2$ shown with the side view (Se–Ta–Se layers) and (b) top view. (c) Schematic illustration of the CVT setup using a two-chamber fused silica ampoule for the growth of TaSe$_2$. The starting materials were positioned on the source side (T_2), while the substrate was placed on the sink side (T_1), ensuring that $T_2 > T_1$.

modification of the band gap and the onset of magnetism, creating a variety of promising property changes.[31] The synthesis of pure bulk 3R polytype by CVT is still extremely challenging due to the potential formation of mixed 2H and 3R polytypes in products.[7,27] This work presents, for the first time, thermodynamically guided synthesis of pure 3R-TaSe$_2$ NCs on various substrates using a direct CVT approach. Notably, HRTEM investigations of the CVT-grown NCs reveal high crystalline quality, with no evidence of Ta vacancies or Ta self-intercalation. In contrast, such defects were reported in crystals grown by CVD[27] and MBE[28] respectively. These results highlight the advantage of the CVT method for synthesizing high-purity 3R-TaSe$_2$ NCs with superior structural quality and a reduced density of defects. Of particular interest, the prepared 3R-TaSe$_2$ crystals on a SiO$_2$/Si substrate showed a signature of CDWs and a high superconducting critical temperature of 2.2 K. These results establish a direct correlation between growth conditions, substrate choice, and the resulting layer morphology and thickness, providing a framework for tailoring structural quality to enable precise investigations of CDWs and superconductivity.

Experimental section

Materials

A Ta-100 mesh (metals basis 99.98%, Alfa Aesar), Se (99.999%, Alfa Aesar), and sublimated I$_2$ (double sublimed, analytical grade, Merck) were used as starting materials for preparing the targeted compounds. All materials were stored and handled in a glovebox (M Braun; $p(H_2O)/p° < 1$ ppm and $p(O_2)/p° < 1$ ppm).

Preparation and pretreatment of substrates

All wafers were coated with a photoresist layer on the polished surface as a protection during the cutting process and then cut into specific dimension substrates. Following this, they were thoroughly cleaned with acetone and isopropanol by ultrasonic treatment for 10 minutes, and the remaining solvent was removed with compressed nitrogen. Finally, the substrates except mica were annealed in air at 1000 °C for one hour and allowed to naturally cool down to room temperature.[32]

Synthesis of TaSe$_2$ NCs by CVT

Two-chamber fused silica ampoules (internal diameter of the diffusion tube $d_i = 10$ mm, diffusion length $s = 12$ cm, neck $d_A \approx 6$ mm, and a volume of 9.4 ml) were used for the CVT experiments (see Fig. 1c). The ampoules were filled with a few milligrams (*ca.* 1–2 mg) of a mixture of Ta and Se in the Ta : Se = 1 : 2 ratio along with *ca.* 1–2 mg of I$_2$ per ampoule as a transport additive. To promote the formation of 2D TaSe$_2$ NCs, the precursor amount was deliberately kept low. Increasing the precursor quantity led to higher supersaturation in the growth zone, which resulted in (i) thicker crystals due to enhanced vertical growth and (ii) increased nucleation and agglomeration on the substrate surface. Therefore, we intentionally used a small precursor amount (1–2 mg of the Ta and Se mixture) and a short transport time (30 minutes) to maintain optimal

supersaturation conditions, prevent vertical growth, and ensure high-quality 2D NCs.

Then, the ampoules were sealed under vacuum with an oxygen–hydrogen flame. To prevent iodine evaporation during sealing, a sponge soaked in liquid nitrogen was used around the source side of the ampoules. The valves were gradually opened, allowing the pressure to stabilize at approximately 2×10^{-3} mbar. The CVT growth process involved varying conditions, including a temperature gradient (ΔT), growth duration (t_{dwell}), and the amount of starting materials. The growth procedure was repeated multiple times under identical conditions, consistently yielding phase-pure 3R-$TaSe_2$ NCs on SiO_2/Si with a comparable morphology.

Characterization of $TaSe_2$ NCs

Preparation of the TEM lamella. Lamellas were prepared from selected crystals by focused ion beam (FIB) cutting. The preparation process was conducted using a Helios 5 CX (Thermo Scientific) system. Initially, a 10 nm carbon layer was deposited onto the sample *via* sputter coating. This was followed by electron beam-induced deposition (EBID) and ion beam-induced deposition (IBID) to provide enhanced protection and structural stability. FIB milling was performed at an acceleration voltage of 30 kV with a current of 2.5 nA to create the initial trenches. Final polishing was carried out using a reduced current to minimize sample damage and achieve superior surface quality.

Light microscopy (OM). OM images of the as-grown NCs were captured using an optical microscope (Keyence VHX-7000) equipped with a VHX-7020 CMOS image sensor under ambient conditions.

Scanning electron microscopy (SEM) and energy dispersive X-ray spectroscopy (EDX). Morphological and compositional analyses were carried out using SEM at varying magnifications in conjunction with EDX (a ZEISS microscope equipped with an Oxford Instruments detector). Elemental mapping was performed to evaluate the spatial distribution of the constituent elements across the NCs. The elemental composition of the NCs was determined using AZtecWave software (v. 6.1 SP2).

Micro-Raman spectroscopic investigations. For Raman investigations, a "T64000 spectrometer" (Horiba Jobin Yvon) was utilized. The measurements were conducted under 532 nm laser excitation at room temperature using a 1800 gr per mm^{-1} grating.

Transmission electron microscopy (TEM). TEM analysis was performed on the prepared lamella. High-resolution TEM (HRTEM) measurements were carried out using an "FEI Titan[3] 80–300" instrument (ThermoFisher Scientific) operated at an acceleration voltage of 300 kV.

Atomic force microscopy (AFM). Under ambient conditions, the thicknesses of $TaSe_2$ NCs were measured by AFM using a TESPA-V2 cantilever in tapping mode on a "Dimension ICON" (Bruker, USA). The raw data were analyzed using "Nanoscope Analysis" software, version 1.8.

Magneto-transport properties. Magneto-transport measurements were performed on relatively thick (~200 nm range) individual nanoflakes connected with Ti/Au ohmic contacts patterned by e-beam lithography and metal lift-off in an unetched Hall-bar geometry. The samples were mounted onto the cold finger of an Oxford [3]He Heliox system fitted into the bore of an 18 T superconducting magnet. The resistance was measured using ac lock-in amplifiers (f = 32 Hz) in a current–polarisation configuration with a 5 µA maximum current, and the magnetic field was applied perpendicular to the sample plane.

Theoretical basis

A simulation of the vapor pressures of relevant species and the corresponding condensed phases in thermodynamic equilibrium was performed in order to estimate suitable conditions for the CVT growth of $TaSe_2$ NCs, using iodine as a transport additive. The results of these simulations are shown in Fig. 2. Details of the used thermodynamic data and the procedures of their estimations can be found in the SI.

In order to enable volatilization of the tantalum of $TaSe_2$ to perform CVT, TaH_5 (g) (H = Cl, Br, and I) are known to be by far the most stable gaseous tantalum halide species, while other potential gaseous tantalum compounds such as TaO_2 (g) require conditions that are incompatible with the presence of $TaSe_2$ (s) and would oxidize the latter. According to the simulations, CVT of $TaSe_2$ should be possible at even lower temperatures compared to the case of TaS_2, being a consequence of its higher free enthalpy of formation in combination with a basically identical transport mechanism:

$$TaSe_2 \text{ (s)} + 2.5 \text{ } I_2 \text{ (g)} \rightleftharpoons TaI_5 \text{ (g)} + Se_2 \text{ (g)}$$
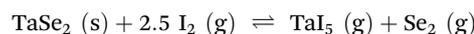
However, due to the lack of accurate thermodynamic data for the full description of all condensed $TaSe_x$ phases (in particular, for the main compound $TaSe_2$), the simulated vapor pressures in Fig. 2 may contain some inaccuracies, especially at the lower temperatures.

Despite the fact that $TaSe_2$ is known to be TMD that can feature metal self-intercalation leading to off-stoichiometric compounds $Ta_{1+x}Se_2$, the endothermic nature of their CVT transport reaction would typically lead to a decrease in the off-stoichiometric parameter x, particularly when a metal-rich source compound is used.[33] Therefore, using stoichiometric mixtures of Ta : Se with a 1 : 2 ratio as starting materials, CVT experiments should result in the growth of stoichiometric $TaSe_2$ in the sink during actual experiments.

Results and discussion

Optimization of growth conditions for the 3R-$TaSe_2$ NCs

Realizing high-quality $TaSe_2$ NCs by CVT requires a simultaneous tuning of various synthesis conditions. In this study, we systematically investigated the effect of growth temperature on $TaSe_2$ formation across different substrates, including such as SiO_2/Si, *c*-sapphire, and mica. Based on our thermodynamic
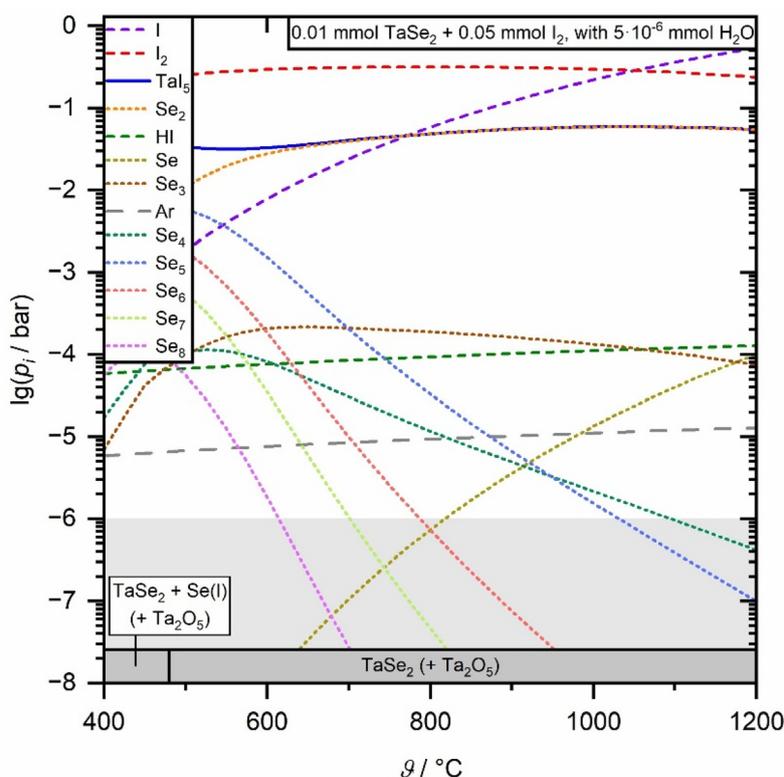
Fig. 2 Simulated temperature-dependent partial pressures of vapor species above 0.01 mmol TaSe$_2$ in combination with 0.05 mmol I$_2$ and 5 × 10^{-6} mmol H$_2$O traces, filling a volume of 9.4 mL. The parameters were selected to be close to the performed growth experiments. The grey area marks partial pressures that are considered too low for macroscopic transport processes.

simulations, we initially choose the growth temperature of 550 °C as a temperature for crystal growth on all studied substrates, while maintaining a constant growth duration of 30 minutes. Importantly, the substrate type exhibited a pronounced influence on the growth behavior and morphology of the resulting TaSe$_2$ NCs, underscoring its essential role in the synthesis process. On SiO$_2$/Si (Fig. 3a), the TaSe$_2$ NCs exhibited a predominantly flat, hexagonal shape, with domain sizes reaching up to 30 μm, uniformly distributed on the surface. In contrast, on c-sapphire (Fig. 3b), the screw dislocation/spiral growth mode was dominant, with well-defined hexagonal crystal shapes. In this case, lateral and layer-by-layer growth is likely inhibited, while spiral growth driven by screw dislocations is preferred. This behavior may be attributed to the crystalline nature of the c-sapphire substrate, which promotes the spiral growth of TaSe$_2$ through an epitaxial alignment with the substrate lattice.[34] Notably, this substrate also promoted simultaneously vertically and horizontally aligned crystals. On mica (Fig. 3c), NCs of both small and large domain sizes were observed, exhibiting flat half-hexagonal and truncated triangular morphologies.

The effect of growth temperature was also studied. Reducing the growth temperature below 500 °C resulted in the formation of nucleation points for crystal growth on SiO$_2$/Si and c-sapphire (Fig. 4a and b). This may be attributed to weak

supersaturation during the induction period of vapor transport, decreasing the likelihood of NC formation. On mica, crystals appeared but exhibited thermal degradation and were relatively thick (Fig. 4c). Conversely, when the growth temperature was gradually increased to 650 °C, the transport rate further increased, leading to the formation of larger crystals (several μm in size), although thermal degradation was also observed.

Interestingly, the TaSe$_2$ NCs grown on the c-sapphire substrate under optimal growth conditions (growth temperature = 550 °C with t_{dwell} = 30 minutes) exhibited different growth mechanisms on the same substrate area: non-spiral (Fig. 5a) and screw dislocation-driven spiral (Fig. 5b and c). This phenomenon might be partially attributed to a temperature gradient across the substrate, creating relatively hotter and colder zones at opposite ends. In the higher temperature zone, crystal growth is limited due to enhanced desorption or decreased supersaturation, whereas in the lower temperature zone, growth is favored, resulting in preferential crystal nucleation and growth. The growth mechanism of TaSe$_2$ on different substrates is schematically illustrated in Fig. 5d. Initially, nucleation points or seeds were formed, which then expanded in substrate-dependent ways. This variation in growth behavior highlights the influence of substrate type on the nucleation and morphology of TaSe$_2$ crystals.

A thickness of around 75 nm was measured for the TaSe$_2$ NC on the SiO$_2$/Si substrate by AFM, indicating multilayer
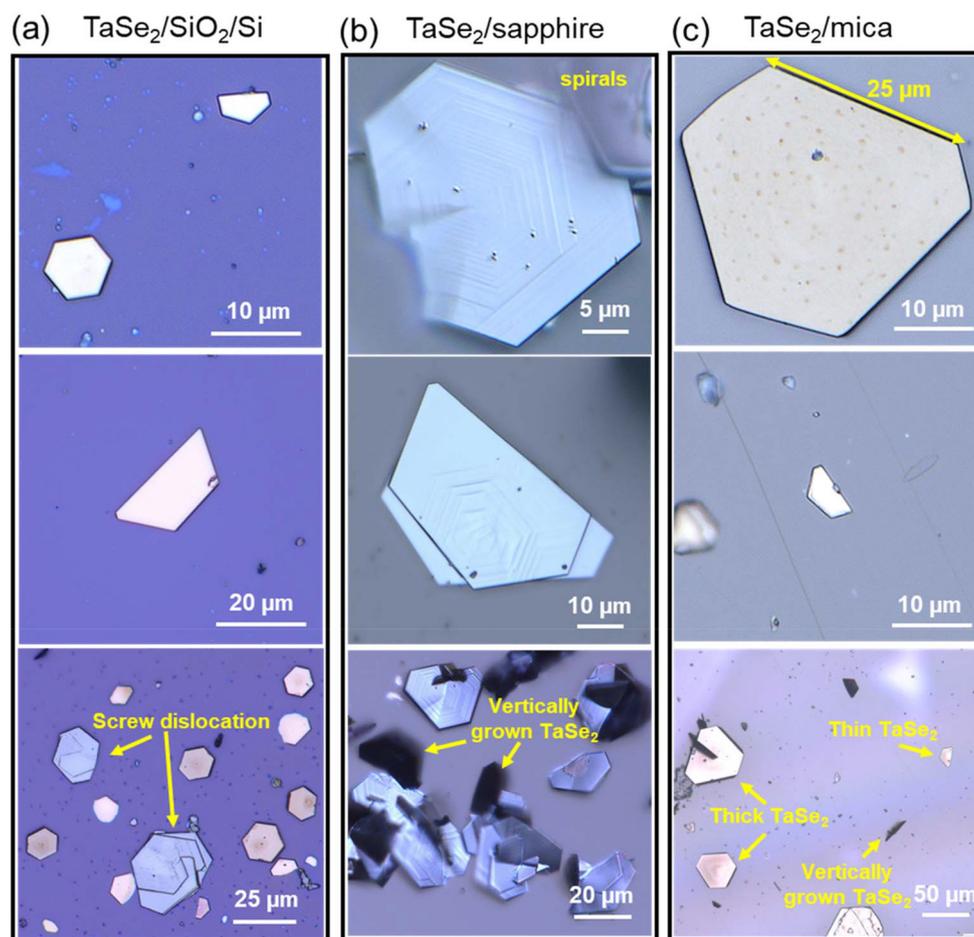
Fig. 3 OM images of TaSe$_2$ NCs stacked in different sizes and morphologies on the (a) SiO$_2$/Si, (b) c-sapphire, and (c) mica substrates under the same growth conditions (growth temperature = 550 °C with t_{dwell} = 30 minutes).
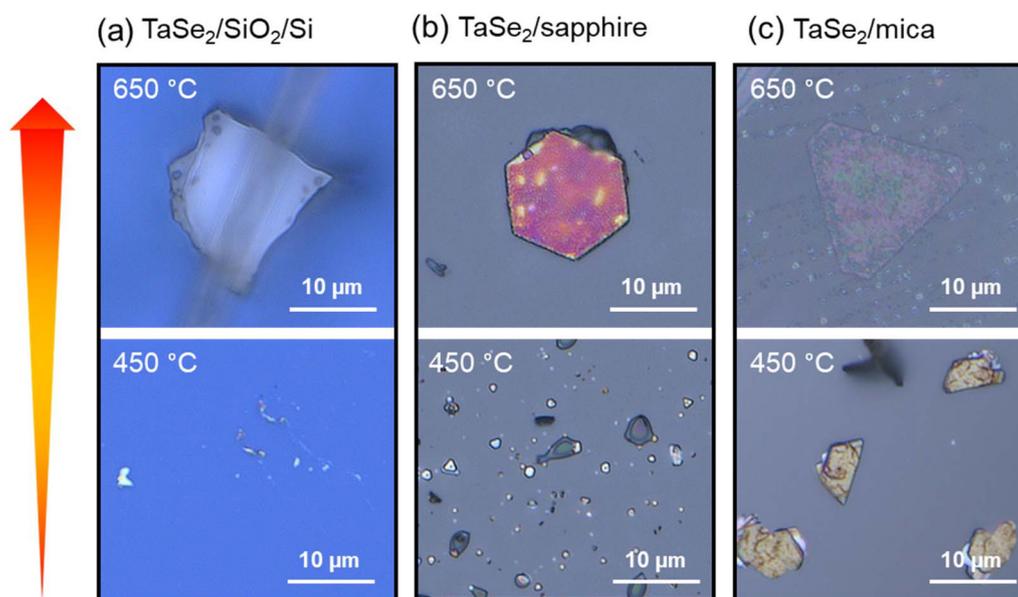

Fig. 4 OM images of TaSe$_2$ NCs grown at different growth temperatures on the (a) SiO$_2$/Si, (b) c-sapphire and (c) mica substrates, while maintaining the same growth time (t_{dwell} = 30 minutes).
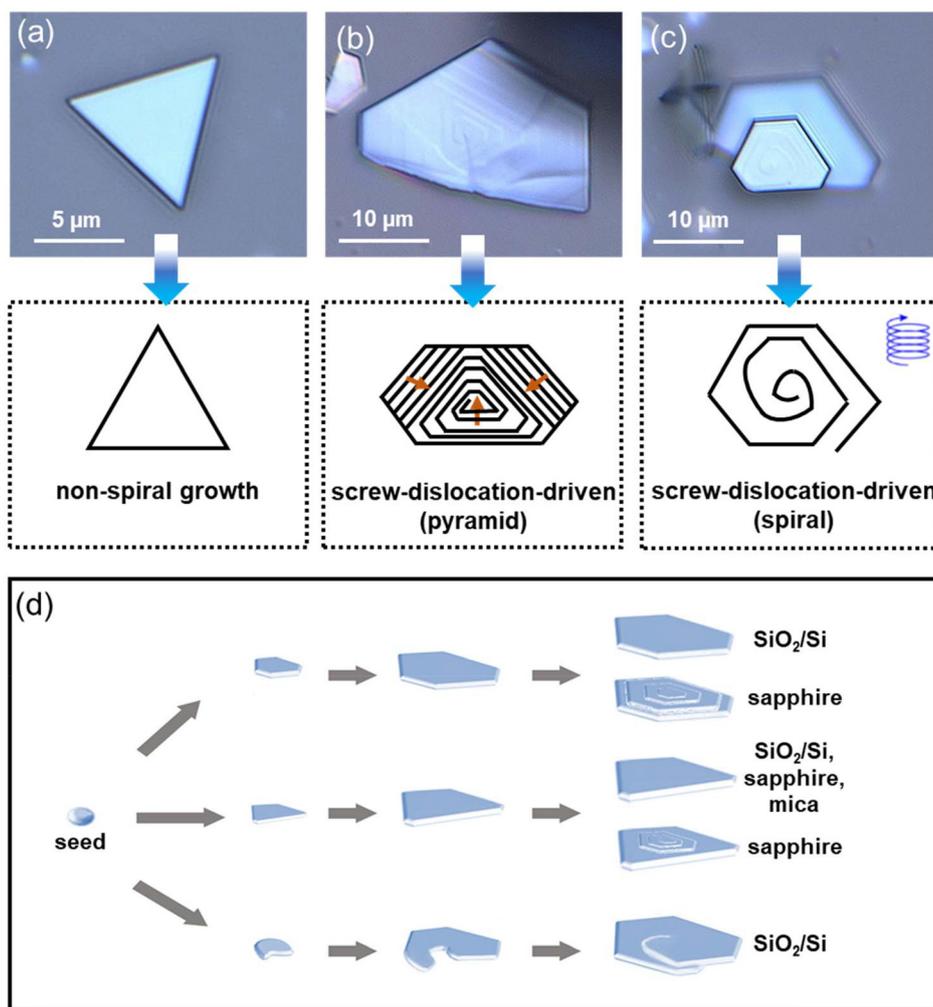
Fig. 5 OM images of TaSe$_2$ NCs on the c-sapphire substrate under the same growth conditions, along with a schematic illustration of the formation mechanisms. (a) Non-spiral, (b) pyramid-like growth driven by screw dislocation, (c) spiral-shaped growth driven by screw dislocation, and (d) schematic representation illustrating the growth mechanism for growing TaSe$_2$ NCs on different substrates.
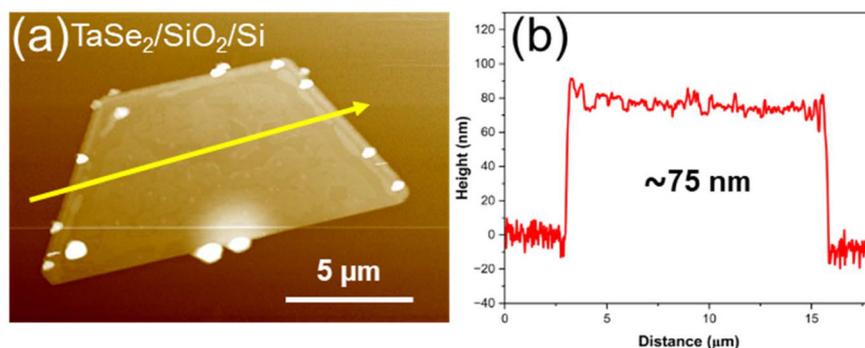

Fig. 6 (a and b) AFM and height profile (along the marked yellow line) images of TaSe$_2$ NC with 75 nm thickness on the SiO$_2$/Si substrate.

crystal growth (Fig. 6a and b). On the c-sapphire substrate, the height of the crystals typically reached the sub-micron level (see Fig. S1 of the SI). The morphology and elemental composition of the TaSe$_2$/SiO$_2$/Si and TaSe$_2$/mica crystals were also examined through SEM-EDX, as shown in Fig. S2 and S3,

respectively. The SEM results showed half-hexagonal or complete hexagonal crystals with variable thicknesses. On the other hand, the EDX data confirmed good matching between the measured atomic percentages of Ta and Se and the targeted TaSe$_2$ composition. To further verify the compositional

uniformity of the synthesized NCs, EDX mapping was performed on the representative 3R-TaSe₂ NCs grown on the SiO₂/Si substrate (Fig. S4). The elemental maps confirm a homogeneous spatial distribution of Ta and Se across the entire crystal area, with no detectable elemental segregation within the instrumental sensitivity. In addition, point EDX analyses acquired at multiple locations on individual NCs (Fig. S4 and S5) yield nearly consistent Ta : Se atomic ratios (close to 1 : 2), further confirming chemical stoichiometry and the absence of foreign impurities. In the following discussion, we focus on investigating the $TaSe_2$ grown on the SiO₂/Si substrate, since it is – compared to c-sapphire or mica – widely used in electronic and optoelectronic device fabrication due to its compatibility with standard microfabrication processes.[2,35]

Investigations of $TaSe_2$ grown on the SiO₂/Si substrate

To determine the crystal structure of $TaSe_2$ NCs grown on the SiO₂/Si substrate, cross-sectional TEM investigations were carried out. For this purpose, a TEM lamella was cut out from a typical NC by FIB milling. The HRTEM image and the corresponding Fourier transform (FT) image shown in Fig. 7a and b demonstrate a high crystallinity of the investigated $TaSe_2$ NC. The FT image agrees with the simulated diffraction pattern of the 3R-TaSe₂ crystal structure oriented in the [100] zone axis (ICSD 24315, R3m space group). This match is also illustrated by comparing the zoom-in image of the HRTEM micrograph (Fig. 7c) with the unit cell model (Fig. 7d). Overall, TEM investigations confirm the formation of a 3R-TaSe₂ polytype on the SiO₂/Si substrate, agreeing well with the Raman investigations shown in Fig. S6. To further explore the physical properties of the as-grown 3R-TaSe₂, magneto-transport measurements were conducted on a 200 nm-thick crystal in a four-probe configuration. The temperature dependence of the longitudinal resistance shows a metal-like behavior with a residual resistance ratio $R(300 \text{ K})/R(4 \text{ K}) = 6.3$, as well as the signature of the CDW transition (slope change at around 100 K) and of superconductivity below 2.2 K (see Fig. 8a), in good agreement with a previous study on CVD-grown 3R-TaSe₂.[27] The transition to the superconducting state spans over a rather broad range, between 2.2 K and 800 mK (see Fig. 8a, bottom inset), suggesting some inhomogeneous properties due to disorder. At 500 mK, this bulk superconductivity is destroyed by applying a small magnetic field, with a critical induction of about 1T (Fig. 8b), and the high-field magneto-resistance shows a quadratic behavior $\Delta R = (\mu B)^2$, where μ is the carrier mobility. Similar findings have been reported in the 3R-TaSe₂ polytype, which may be attributed to the formation of vortices upon applying a perpendicular magnetic field, resulting in dissipation and inhibition of superconductivity.[36,37] This transition is also
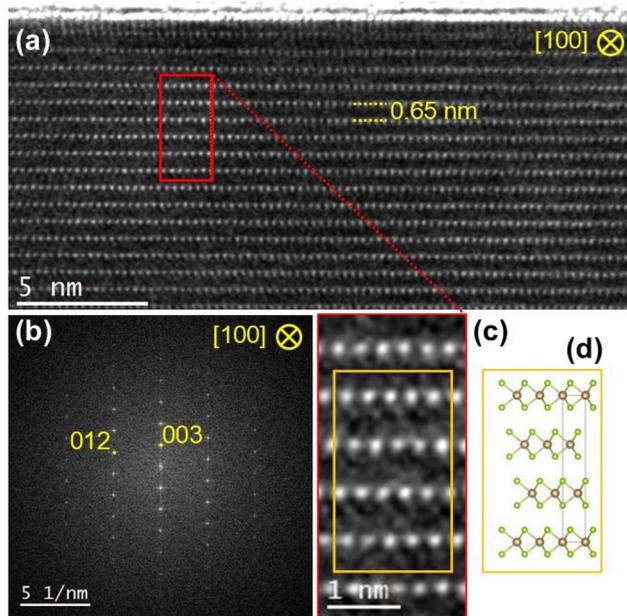

Fig. 7 Cross-sectional HRTEM of 3R-TaSe₂ NC on SiO₂/Si. (a) HRTEM image recorded in the [100] zone axis orientation close to the surface of a 100 nm thick crystal. The c-axis points in the vertical direction. (b) Fourier transform of the HRTEM image (a) with indexed 012 and 003 reflections according to the trigonal space group R3m (ICSD 24315). (c) Zoom-in image at the position marked by the red box in (a). (d) A unit cell model of 3R-TaSe₂ with the Ta atoms in purple gold and the Se atoms in green.
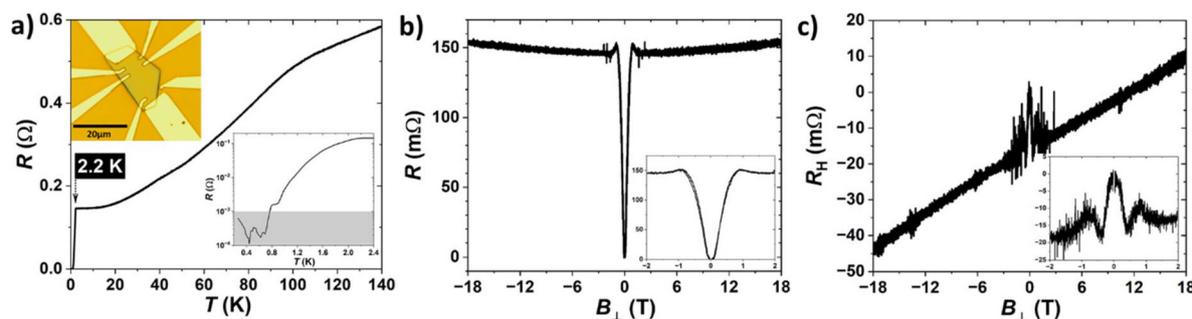

Fig. 8 Magneto-transport properties of a 200 nm-thick 3R-TaSe₂ NC. (a) Temperature dependence of the longitudinal resistance. The top inset is an OM image of the flake connected to Ti/Au contacts, while the bottom inset shows the very-low temperature behavior on a logarithmic scale. The grey zone corresponds to the resolution limit. (b and c) Longitudinal and transverse magneto-resistance under a magnetic induction applied perpendicular to the sample plane, as measured at around 500 mK. The insets show the low-field behavior.

observed in the low-field transverse magneto-resistance, followed by the standard linear Hall response at higher magnetic fields (Fig. 8c). The high-field data give access to the carrier density of 2.1×10^{22} cm^{-3} (Hall) and the carrier mobility of 130 cm^2 V^{-1} s^{-1} (longitudinal magneto-resistance). The superconducting critical temperature (T_c) observed here (2.2 K) is notably higher than that reported for the 1T and 2H polytypes of TaSe$_2$, as well as for the 3R-TaSe$_2$ NCs with 7 nm thickness prepared by CVD ($T_c \approx 1.6$ K).[27] However, it should be noted that the observed Ta vacancies and line defects in the CVD-grown crystals together with the substrate-induced strain at a low thickness might influence the T_c. Tanaka *et al.* reported T_c values up to 3 K for thin films of self-intercalated 3R-Ta$_{1+x}$Se$_2$, which gradually decreased with reduced thickness.[28] In contrast, both TEM and EDX analyses of the 3R-TaSe$_2$ NCs studied here revealed no evidence of Ta self-intercalation or noticeable Ta vacancies, suggesting that the enhanced T_c may arise from dimensionality effects[16] and minimal structural defects.

Future work will focus on determining the precise structural phase of CVT-grown TaSe$_2$ on *c*-sapphire and mica substrates and investigating whether screw dislocations or other extended defects influence the superconducting properties.

Conclusions

In conclusion, we report, for the first time, the synthesis of highly crystalline 3R-TaSe$_2$ NCs on various substrates (SiO$_2$/Si, *c*-sapphire, and mica) using a thermodynamically optimized CVT approach. Distinct screw dislocation-driven growth morphologies were observed on *c*-sapphire, whereas a layer-by-layer growth mechanism was preferred on mica. On the SiO$_2$/Si substrates, both growth modes were identified, highlighting the critical role of growth conditions and substrate choice in tailoring the structural properties of 3R-TaSe$_2$ NCs. EDX mapping and point analyses confirm a homogeneous distribution of Ta and Se across the crystals, with nearly consistent Ta : Se ratios and no detectable secondary phases or impurities, demonstrating high chemical uniformity. Interestingly, a transition due to CDWs was observed by charge transport measurements at around 100 K, and superconductivity was evidenced below 2.2 K. A deeper understanding of the initial growth stages is a key aspect to control the morphological evolution of these high-quality NCs, enabling the investigation of their novel physical and electronic properties at the nanoscale.

Author contributions

Conflicts of interest

The authors declare that there are no competing interests.

Abbreviations

CVT	Chemical vapor transport
AFM	Atomic force microscopy
EDX	Energy dispersive X-ray spectroscopy
OM	Optical microscopy
SEM	Scanning electron microscopy
HRTEM	High-resolution transmission electron microscopy
TMDs	Transition metal dichalcogenide(s)
FIB	Focused ion beam
EBID	Electron beam-induced deposition
IBID	Ion beam-induced deposition
FT	Fourier transform
2D	Two-dimensional
NCs	Nanocrystal(s)
CDW	Charge density wave
MBE	Molecular beam epitaxy
CVD	Chemical vapor deposition
SI	Supporting information
TM	Transition metal
X	Chalcogen
H	Halide(s).

Data availability

Acknowledgements

References

1 B. Sipos, *et al.*, From Mott state to superconductivity in 1T-TaS2, *Nat. Mater.*, 2008, **7**(12), 960–965.

2 Y. Yu, *et al.*, Gate-tunable phase transitions in thin flakes of 1T-TaS2, *Nat. Nanotechnol.*, 2015, **10**(3), 270–276.

3 G. Liu, *et al.*, A charge-density-wave oscillator based on an integrated tantalum disulfide–boron nitride–graphene device operating at room temperature, *Nat. Nanotechnol.*, 2016, **11**(10), 845–850.

4 R. Hovden, *et al.*, Atomic lattice disorder in charge-density-wave phases of exfoliated dichalcogenides (1T-TaS2), *Proc. Natl. Acad. Sci. U. S. A.*, 2016, **113**(41), 11420–11424.

5 J. van Wezel, *et al.*, Effect of charge order on the plasmon dispersion in transition-metal dichalcogenides, *Phys. Rev. Lett.*, 2011, **107**(17), 176404.

6 S. Sun, *et al.*, Direct observation of an optically induced charge density wave transition in 1T-TaSe2, *Phys. Rev. B: Condens. Matter Mater. Phys.*, 2015, **92**(22), 224303.

7 R. Samnakay, *et al.*, Zone-folded phonons and the commensurate–incommensurate charge-density-wave transition in 1T-TaSe2 thin films, *Nano Lett.*, 2015, **15**(5), 2965–2973.

8 L. Li, *et al.*, Controlling many-body states by the electric-field effect in a two-dimensional material, *Nature*, 2016, **529**(7585), 185–189.

9 M. Porer, *et al.*, Non-thermal separation of electronic and structural orders in a persisting charge density wave, *Nat. Mater.*, 2014, **13**(9), 857–861.

10 Y. I. Joe, *et al.*, Emergence of charge density wave domain walls above the superconducting dome in 1T-TiSe2, *Nat. Phys.*, 2014, **10**(6), 421–425.

11 J.-P. Peng, *et al.*, Molecular beam epitaxy growth and scanning tunneling microscopy study of TiSe2 ultrathin films, *Phys. Rev. B: Condens. Matter Mater. Phys.*, 2015, **91**(12), 121113.

12 J. Wang, *et al.*, Controlled Synthesis of Two-Dimensional 1 T-TiSe2 with Charge Density Wave Transition by Chemical Vapor Transport, *J. Am. Chem. Soc.*, 2016, **138**(50), 16216–16219.

13 M. Langer, *et al.*, Giant frictional dissipation peaks and charge-density-wave slips at the NbSe2 surface, *Nat. Mater.*, 2014, **13**(2), 173–177.

14 M. M. Ugeda, *et al.*, Characterization of collective ground states in single-layer NbSe2, *Nat. Phys.*, 2016, **12**(1), 92–97.

15 X. Xi, *et al.*, Strongly enhanced charge-density-wave order in monolayer NbSe2, *Nat. Nanotechnol.*, 2015, **10**(9), 765–769.

16 X. Xi, *et al.*, Ising pairing in superconducting NbSe2 atomic layers, *Nat. Phys.*, 2016, **12**(2), 139–143.

17 S. Manzeli, *et al.*, 2D transition metal dichalcogenides, *Nat. Rev. Mater.*, 2017, **2**(17033).

18 F. Di Salvo, *et al.*, Preparation and properties of a new polytype of tantalum disulfide (4Hb-TaS2), *J. Phys. Chem. Solids*, 1973, **34**(8), 1357–1362.

19 E. Figueroa, *et al.*, Physical properties of 6R-TaS2, *J. Solid State Chem.*, 1995, **114**(2), 486–490.

20 A. Thompson, The synthesis and properties of 6R-TaS2, *Solid State Commun.*, 1975, **17**(9), 1115–1117.

21 S. Nagata, *et al.*, Superconductivity in the layered compound 2H-TaS2, *J. Phys. Chem. Solids*, 1992, **53**(10), 1259–1263.

22 C. Su, *et al.*, Controlled growth of 3R phase niobium diselenide and its properties, *J. Colloid Interface Sci.*, 2024, **670**, 28–40.

23 Z. H. Peng, *et al.*, 3R-stacked transition metal dichalcogenide non-local metasurface for efficient second-harmonic generation, *Nat. Photonics*, 2025, 1–9.

24 D. Yang, *et al.*, Inversion symmetry broken 2D 3R–MoTe2, *Adv. Funct. Mater.*, 2018, **28**(26), 1800785.

25 Y. Gong, *et al.*, Reconfigurable and nonvolatile ferroelectric bulk photovoltaics based on 3R-WS2 for machine vision, *Nat. Commun.*, 2025, **16**(1), 230.

26 Z. Zeng, *et al.*, Controlled vapor growth and nonlinear optical applications of large–area 3R phase WS2 and WSe2 atomic layers, *Adv. Funct. Mater.*, 2019, **29**(11), 1806874.

27 Y. Deng, *et al.*, Controlled growth of 3R phase tantalum diselenide and its enhanced superconductivity, *J. Am. Chem. Soc.*, 2020, **142**(6), 2948–2955.

28 Y. Tanaka, *et al.*, Superconducting 3R-Ta1+xSe2 with Giant In-Plane Upper Critical Fields, *Nano Lett.*, 2020, **20**(3), 1725–1730.

29 Z. Xie, *et al.*, Ising Superconductivity and Signatures of Orbital FFLO State in Non–Centrosymmetric 3R–TaSe2 Thin Flakes, *Adv. Funct. Mater.*, 2025, **35**(32), 2501453.

30 X. Huang, *et al.*, Observation of two-dimensional type-II superconductivity in bulk 3R-TaSe2 by scanning tunneling spectroscopy, *J. Phys. Chem. Lett.*, 2023, **14**(32), 7235–7240.

31 A. C. Neto and K. Novoselov, New directions in science and technology: two-dimensional crystals, *Rep. Prog. Phys.*, 2011, **74**(8), 082501.

32 M. Yoshimoto, *et al.*, Atomic–scale formation of ultrasmooth surfaces on sapphire substrates for high–quality thin–film fabrication, *Appl. Phys. Lett.*, 1995, **67**(18), 2615–2617.

33 H. Schäfer and W. Fuhr, Beiträge zur chemie der elemente niob und tantal: XLIII. Verbindungen des niobs mit P, As, Sb, S, Se, Te. Synthese und chemischer transport, *J. Less-Common Met.*, 1965, **8**(6), 375–387.

34 C. J. Chen, *et al.*, Tunable Electron Correlation in Epitaxial 1T–TaS2 Spirals, *Adv. Mater.*, 2025, **37**(6), 2413926.

35 C. Zhu, *et al.*, Light-tunable 1T-TaS2 charge-density-wave oscillators, *ACS Nano*, 2018, **12**(11), 11203–11210.

36 Y. Cao, *et al.*, Unconventional superconductivity in magic-angle graphene superlattices, *Nature*, 2018, **556**(7699), 43–50.

37 M. Tinkham, *Introduction to superconductivity*, Courier Corporation, 2004.